SUPPORTING INFORMATION

Circularly polarized luminescence under near-UV excitation and structural elucidation of a Eu complex

Francesco Zinna, Claudio Resta, Sergio Abbate, Ettore Castiglioni, Giovanna Longhi, Placido Mineo, Lorenzo Di Bari*

Experimental

Instruments and methods

NMR were performed with a Varian spectrometer operating at 600, 150 and 79 MHz for ^{1}H, ^{13}C and ^{133}Cs respectively, inversion recovery and 2D experiments were performed using standard pulse sequences, a reverse triple resonance ^{1}H, ^{13}C tunable or a direct broadband with z-gradients probe head were used. Temperature was set to 25.0 ± 0.1 °C and in all cases the sample was let equilibrate for at least 10 min before acquisition.

The MALDI-TOF mass spectra were collected with a Voyager DE (PerSeptive Biosystem) equipped with a nitrogen laser (emission at 337 nm for 3 ns) and a flash AD converter (time base 2 ns). In order to avoid fragmentation of the sample, the laser irradiance was maintained slightly above threshold. Each spectrum was an average of 32 laser shots. The MALDI-TOF investigations were performed by loading on the plate 0.4 mmol of matrix, trans-2-[3-(4-tert-butylphenyl)-2-methyl-2propenylidene]-malonitrile (DCTB), and 0.005 mmol of sample, using CH_2Cl_2 as the solvent. For positive MALDI-TOF mass spectra, both 5,10-di(p-dodecanoxyphenyl)-15,20-di(p-hydroxyphenyl) porphyrin ($C_{68}H_{78}N_4O_4$, 1014 Da), tetrakis(p-dodecanoxyphenyl)porphyrin ($C_{92}H_{126}N_4O_4$, 1350 Da) and a PEG sample of known structure were used as external standards for m/z calibration. Instead, for negative MALDI-TOF spectra, fullerene-[60] ($C_{60,}$ 720 Da) and 61,61-bis(p-methoxyphenyl)methano-1,2-fullerene[60] ($C_{75}H_{14}O_2$, 946 Da) were used as external standards for m/z calibration. The MALDI-TOF mass spectra were elaborated with Grams software (ver. 3.04), from Perseptive Biosystems.

UV-Vis spectra were recorded with a JASCO V-650 spectrophotometer, ECD spectra were recorded with a JASCO J-710 spectropolarimeter.

Luminescence measurements were carried on with a JASCO FP-8200 spectrofluorometer with emission bandpass of 2.5 nm using a custom built 180° solid film sampling device. Wavelength calibration had been checked with the built-in low pressure Hg-source. CPL spectra were recorded with a home-made apparatus described in Reference [1] and [2]. The 370 nm excitation radiation, with 20 nm bandpass, was provided, using an optical liquid guide, by a JASCO FP-8200 spectrofluorometer, while the emission bandpass has been kept at 2 nm for all the experiments. Solutions samples were measured at 90° with a 2x10 mm quartz cell, while for film samples a 180° geometry has been used. The presence of artifacts due to linear polarization components has been excluded by demodulating the signal at twice the frequency of photoelastic modulator, with an additional 100 KHz lock-in amplifier.

The ligand geometry used as the PERSEUS calculation input was determined optimizing a Na^+ anion of trifluoromethylcarvonate at DFT level with B3LYP functional and 6-31G* basis set using Gaussian.[S3]

All the syntheses were carried under N_2 atmosphere in oven dried glassware using standard Schlenk techniques.

Synthesis of heptafluorobutyrylcarvone

To a solution of 7.5 mL (53 mmol) of $^{i}Pr_2NH$ in 60 mL of distilled diethyl ether 21.6 mL (53 mmol) of $^{n}BuLi$ 2.5 M in 100 mL of ether were slowly dropped; after a hour, the system was cooled to -90 °C, 8.0 mL (53 mmol) of (±)-carvone and, after additional two hours, 9.7 mL (56 mmol) of ethyl heptafluorobutyrate were added. The resulting mixture was allowed to warm to room temperature under stirring overnight and then it was hydrolyzed with 60 mL of HCl ≈3M and extracted with ether (2x100 mL). The recombined organic phases were washed with water until neutrality (5x100 mL), dried on Na_2SO_4 and the solvent was evaporated under reduced pressure. The crude product was purified by flash chromatography (SiO_2; CH_2Cl_2/petroleum ether:8/2) to afford the product as a reddishbrown liquid (5.5 g, 30%).

^{1}H-NMR ($CDCl_3$, 25 °C, eno form), δ (ppm): 1.74 (s, 3H); 1.90 (s, 3H); 2.57 (m, 2H); 3.56 (m, 1H); 4.52 (m, 1H); 4.84 (m, 1H); 6.50 (m, 1H); 16.48 (s, 1H).

^{13}C-NMR ($CDCl_3$, 25 °C, eno form), δ(ppm): 15.8 (C-Me); 22.1 (C-Me); 28.5 (C4); 37.9 (C5); 113.1 (C8); 142.8 (C3); 190.3; 195.0.
Negative MALDI-TOF (m/z): 346.2 [M] (Figure S16)
λ_{max}/nm, CH_3CN (ε/$M^{-1}cm^{-1}$): 240 (5640); 313 (2680); 358 (2160).

Preparation of Cs[Ln(hfbcv)$_4$]
To 260 mg (0.75 mmol) of heptafluorobutyrylcarvone in 5 mL of distilled CH_3CN, 254 mg (0.75 mmol) of Cs_2CO_3 were added at 50 °C; after an hour 0.19 mmol of anhydrous $LnCl_3$ were added, and the mixture was stirred for 4 hours at 50 °C. The solvent was removed under reduced pressure and the crude product product was taken up with 2 mL of distilled diethyl ether and filtered through a sintered glass filter (porosity G3). After removing the solvent, 800 mL of petroleum ether were added, and the mixture was allowed to cool down to -10 °C; the supernatant solution was recovered and the solvent was evaporated under reduced pressure.
^{1}H-NMR (CD_3CN, 25 °C, broad singlets)
δ(ppm) (Ln=La): 1.66 (6H); 2.94; 3.27; 3.44; 4.51; 4.64; 6.17.
δ(ppm) (Ln=Ce): 0.28 (3H); 2.77 (3H); 3.52; 5.73; 6.15; 7.54; 8.14.
δ(ppm) (Ln=Pr): -2.67 (3H); 3.39 (3H); 4.35; 4.85; 6.93; 7.47; 8.41; 10.03.
δ(ppm) (Ln=Nd): 0.69 (3H); 2.62 (3H); 3.09; 3.34; 5.51; 5.93; 7.6; 8.19.
δ(ppm) (Ln=Eu): 0.78 (3H); 1.45; 1.55; 1.64; 2.08; 2.82 (3H); 3.11; 3.44.
δ(ppm) (Ln=Tb): -27.21 (3H); 14.81; 21.74 (3H); 25.71; 33.19; 36.03; 41.45; 75.26.
^{13}C-NMR
δ(ppm) (Ln=La): 16.2; 21.1; 40.1; 112.2; 135.9.
δ(ppm) (Ln=Ce): 15.0; 23.4; 31.0; 42.3; 115.0; 133.8.
δ(ppm) (Ln=Pr): 23.9; 33.3; 42.8; 116.0; 134.6.
δ(ppm) (Ln=Nd): 15.2; 22.6; 31.8; 39.2; 114.8; 135.4.
δ(ppm) (Ln=Eu): 18.4; 21.3; 25.3; 43.8; 110.9; 132.8.
Positive MALDI-TOF (Figure S17) of Cs[Eu(hfbcv)$_4$] (m/z): 1666.5 $[M]H^+$
Negative MALDI-TOF (Figure S18) of Cs[Eu(hfbcv)$_4$] (m/z): 345.5, $hfbcv^-$; 1187.3, Eu(hfbcv)$_3$; 1532.6, $[Eu(hfbcv)_4]^-$.

Preparation of Cs[Ln(hfbcv)$_4$]/Ln(hfbcv)$_3$ mixture
$LnCl_3$ (0.13 mmol) and CsCl (0.5 mmol) were dissolved in water (10 mL), simultaneously a Et_3N (0.50 mmol) and hfbcvH (0.50 mmol) solution in $CHCl_3$ (10 mL) was prepared. The two solution were mixed together in a separatory funnel and shaken. The organic phase was recovered, washed with water dried over anhydrous Na_2SO_4. The solvent was evaporated under reduced pressure.

Optical characterization

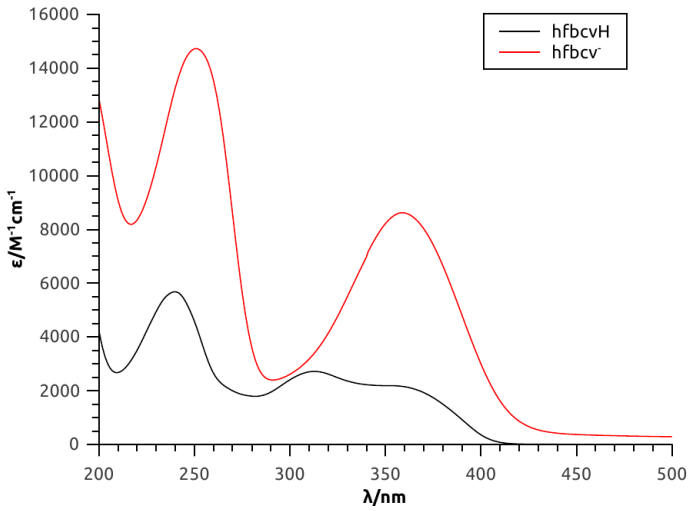

Figure S1: Absorption spectra of hfbcvH (3.9×10^{-3} M) and hfbcv anion (2.0×10^{-3} M) in CH_3CN solution (optical path 0.05 cm).

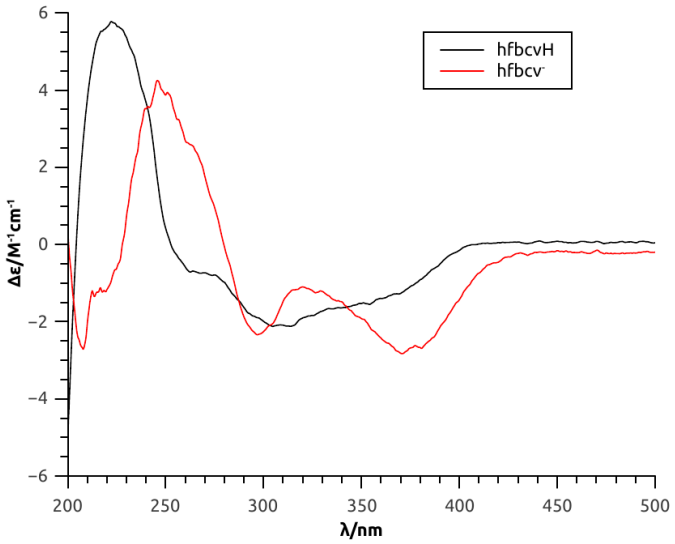

Figure S2: ECD spectra of hfbcvH (3.9×10^{-3} M) and hfbcv$^-$ anion (2.0×10^{-3} M) in CH_3CN solution (optical path 0.05 cm).

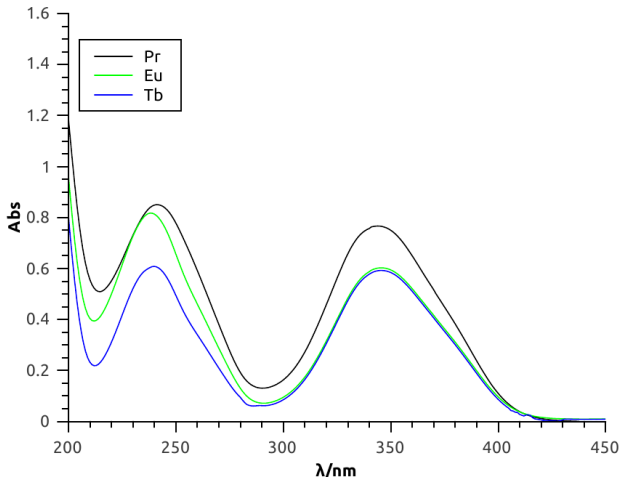

Figure S3: Absorption spectra of $Cs[Ln(hfbcv)_4]$ (Ln=Pr, Eu, Tb) 6.0×10^{-3}M in CH_3CN solution (optical path 0.01 cm).

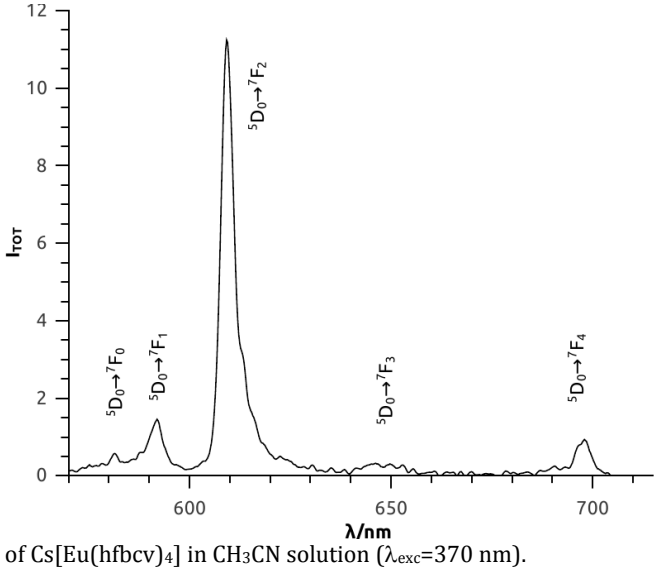

Figure S4: Emission spectrum of Cs[Eu(hfbcv)$_4$] in CH_3CN solution (λ_{exc}=370 nm).

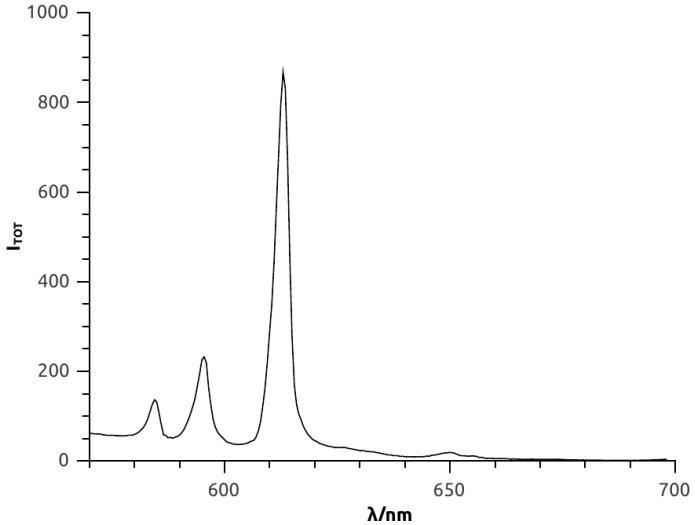

Figure S5: Emission spectrum of Cs[Eu(hfbcv)$_4$] on a quartz plate deposition (λ_{exc}=370 nm).

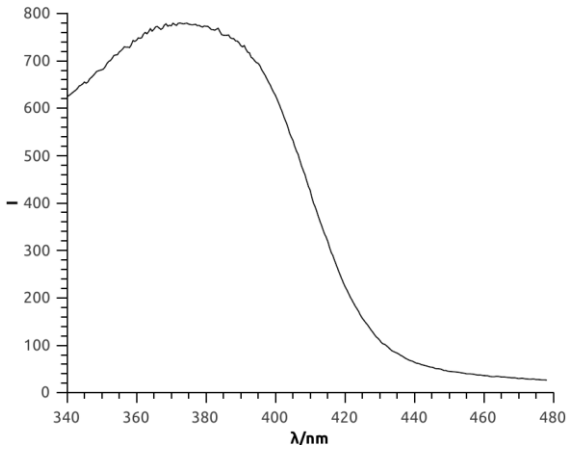

Figure S6: Excitation spectrum of Cs[Eu(hfbcv)$_4$] on a quartz plate deposition (λ_{em}=612 nm).

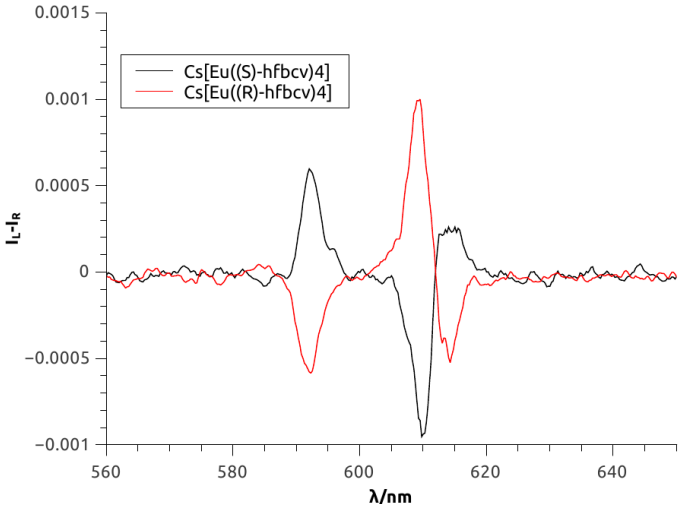

Figure S7: CPL spectra of Cs[Eu((S)hfbcv)$_4$] (black) and Cs[Eu((R)hfbcv)$_4$] (red) in CH_3CN solution.

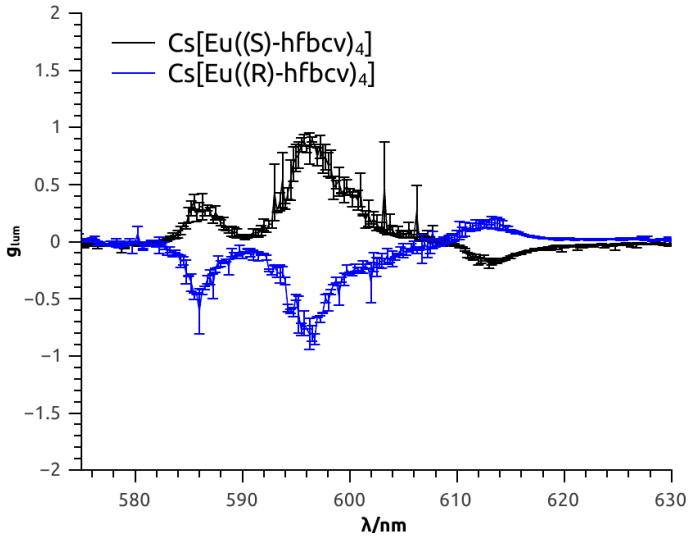

Figure S8: Average values of g_{lum} on three independent measurements as a function of wavelength for Cs[Eu(hfbcv)$_4$] complexes on quartz plate depositions. The bars represent one standard deviation.

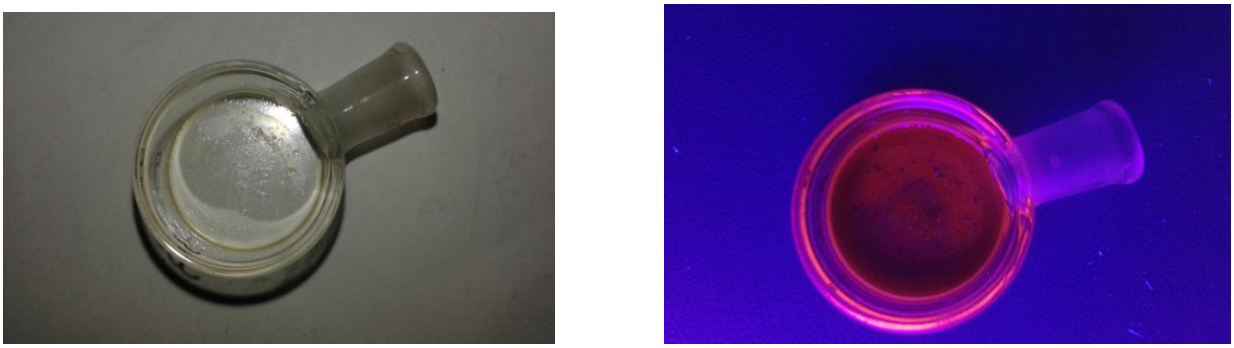

Figure S9: An example of deposition of Cs[Eu(hfbcv)$_4$] on a quartz plate under daylight (left) and 365 nm irradiation (right). The 1 cm quartz cell in the picture has the top window cut off.

NMR structural characterization

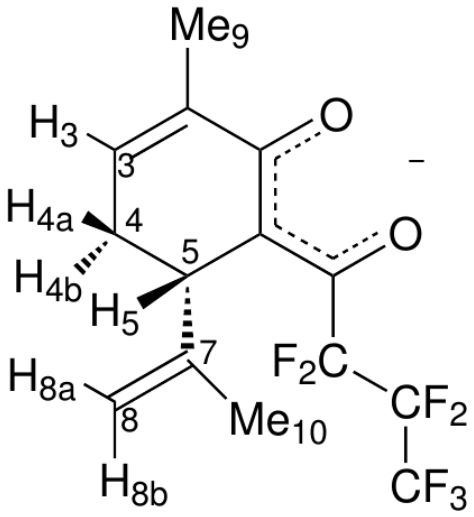

Resonances and isostructurality

Paramagnetic shifts (δ^{para}) were extracted by subtracting the shifts obtained from the diamagnetic Cs[La(hfbcv)$_4$] complex from the observed shifts (δ^{obs}).

$$\delta^{para} = \delta^{obs} - \delta^{dia}$$

Table S1: ^{1}H δ^{para} for the Cs[Ln(hfbcv)$_4$] complexes and diamagnetic references (δ^{dia}) from Cs[La(hfbcv)$_4$].

^{1}H	Pr δ^{para}	Ce δ^{para}	Nd δ^{para}	Eu δ^{para}	Tb δ^{para}	La δ^{dia}
Me$_9$	-4.33	-1.38	-0.97	1.16	-29.11	1.66
Me$_{10}$	1.73	1.11	0.96	-0.88	20.00	1.66
3	2.24	1.37	2.20	-3.06	29.54	6.17
4a	1.08	0.25	0.07	-1.63	11.52	3.27
4b	1.91	/	0.15	-0.86	23.15	2.94
5	4.03	2.29	2.07	-1.99	37.90	3.44
8a	5.39	3.50	2.96	-3.09	70.78	4.64
8b	2.42	1.64	1.42	-1.07	28.36	4.51

Table S2: ^{13}C δ^{para} for the Cs[Ln(hfbcv)$_4$] complexes and diamagnetic references (δ^{dia} from Cs[La(hfbcv)$_4$]).

^{13}C	Pr δ^{para}	Ce δ^{para}	Nd δ^{para}	Eu δ^{para}	La δ^{dia}
C-Me$_9$	-2.1	-6.1	-5.9	-2.7	21.1
C-Me$_{10}$	7.7	7.2	6.4	5.1	16.2
C3	-1.3	-2.1	-0.5	-3.1	135.9
C5	2.7	2.2	-0.9	3.7	40.1
C8	3.8	2.8	2.6	-1.3	112.2

Isostructurality along the investigated part of the series can be assessed plotting the ^{1}H paramagnetic shifts for each resonances of a given lanthanide (δ^{para}*(Ln)*) against the paramagnetic shifts observed for a reference complex, in our case Cs[Pr(hfbcv)$_4$] δ^{para}*(Pr)*.[S4]

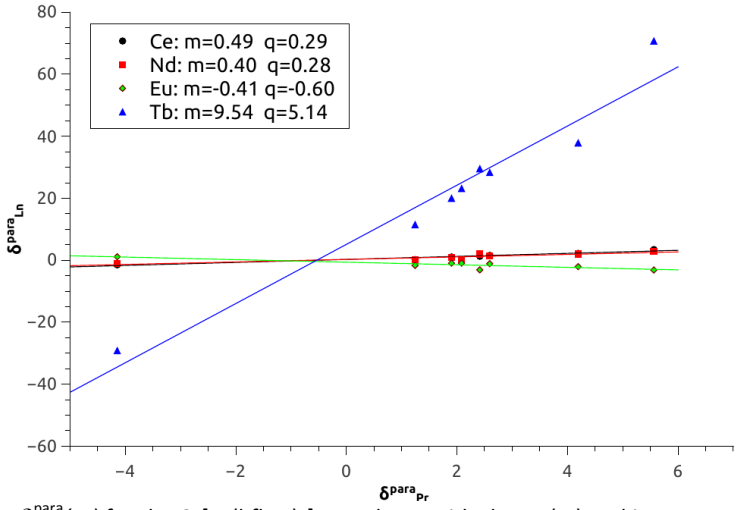

Figure S10: $\delta^{para}(Ln)$ against $\delta^{para}(Pr)$ for the Cs[Ln(hfbcv)$_4$] complexes with slopes (m) and intercepts (q), showing isostructurality. Notice that the lines were not forced through the origin.

The linearity (R^2>0.99) between the obtained m_{Ln} slopes (Figure S10) and the Bleaney C_j constants demonstrates no major crystal field parameter variation from Ce to Eu.

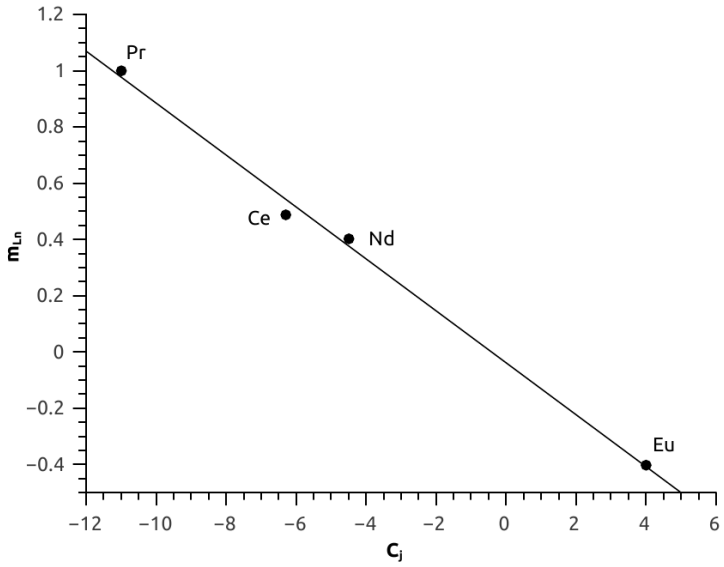

Figure S11: m_{Ln} (see Figure S10) against Bleaney C_j constants.

Fermi contact/pseudocontact separation

Pseudocontact shifts (δ^{PC}) are relevant for structure determination (see below), they are determined by subtracting the Fermi contact shifts (δ^{FC}) from the paramagnetic shift (δ^{para}):

$$\delta^{PC} = \delta^{para} - \delta^{FC}$$

To determine δ^{FC} we used the slopes of the linear interpolations m_{Ln} (Figure S10) through the modified Reilley procedure,[S5] with Pr complex as the reference, since it provides a large $C_j/\langle S_Z \rangle_{Ln}$ ratio.[S5] In our case, the contribution of the Fermi contact shift resulted negligible or very small for both ^{1}H and ^{13}C resonance sets (Table S3).

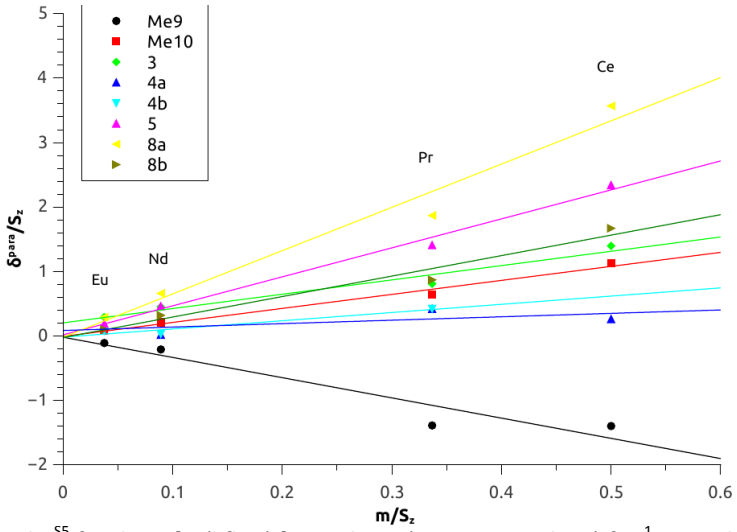

Figure S12: Modified Reilley plot[S5] for the Cs[Ln(hfbcv)$_4$] complexes (Ln= Ce, Pr, Nd, Eu) for ^{1}H Pseudocontact/Fermi contact shift separation.

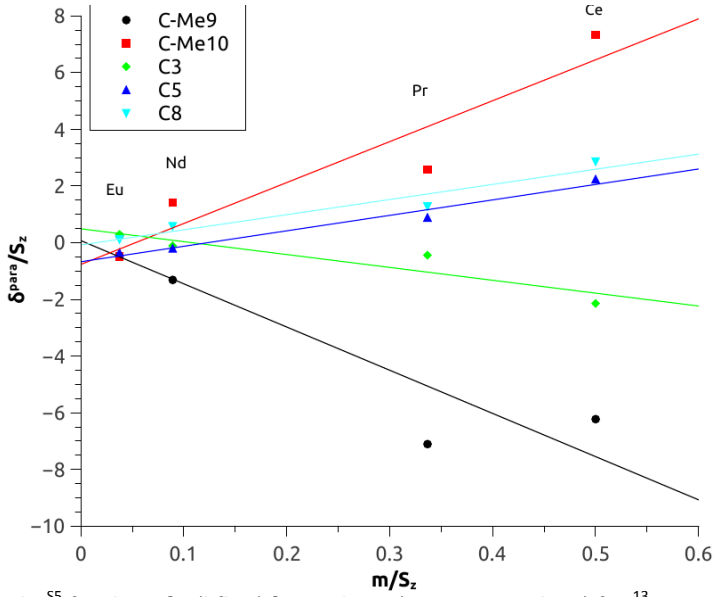

Figure S13: Modified Reilley plot[S5] for the Cs[Ln(hfbcv)$_4$] complexes (Ln= Ce, Pr, Nd, Eu) for ^{13}C Pseudocontact/Fermi contact shift separation.

Structure determination

Pseudocontact shifts contain geometric information. The pseudocontact shift of each observed nucleus *i* is:

$$\delta_i^{PC} = D\,\frac{3\cos^2\vartheta_i - 1}{r_i^3}$$

where ϑ is the angle between the nucleus-Ln vector and the C_4 axis, r_i is the distance between the lanthanide and nucleus *i* and *D* is a parameter related to the anisotropy susceptibility tensor of the complex.

PERSEUS routine takes a guess structure as the input, calculates $\delta^{PC}{}_{exp}$ for each nucleus (using the equation above) and compare the obtained value with the experimental one ($\delta^{PC}{}_{exp}$). Then, by minimizing the functional

$$\sum_i \frac{(\delta^{PC}_{i,calc} - \delta^{PC}_{i,exp})^2}{{\delta^{PC}_{i,exp}}^2}$$

it can determine the best-fitting geometrical parameters.

In a similar way it can use also paramagnetic relaxation rates (ρ^{para}_i) as additional constraints. In fact

$$\rho_i^{para} = \frac{\text{Const}}{r_i^3}$$

Table S3: PERSEUS output: Cs[Pr(hfbcv)$_4$] ^{1}H and ^{13}C-NMR calculated (δ^{PC}_{calc}) and experimental (δ^{PC}_{exp}) pseudocontact shifts, and Fermi contact shifts (δ^{FC}) obtained through modified Reilley procedure.[S5]

Nucleus	δ^{PC}_{calc}	δ^{PC}_{exp}	δ^{FC}
Me$_9$	-4.02	-4.31	-0.02
Me$_{10}$	1.71	1.74	-0.01
3	0.53	2.04	0.20
4a	1.80	1.08	0.01
4b	2.62	1.91	-0.02
5	3.64	4.02	0.02
8a	5.39	5.41	-0.02
8b	2.62	2.44	-0.02
C-Me$_{10}$	2.86	8.46	-0.76
C3	1.38	-1.79	-0.49
C5	6.02	3.17	-0.67
C8	4.31	3.81	-0.01

Table S4: PERSEUS output: Cs[Pr(hfbcv)$_4$] calculated (ρ^{para}_{calc}) and experimental (ρ^{para}_{exp}) relaxation rates, and their residuals ($\Delta\rho = \rho^{para}_{calc} - \rho^{para}_{exp}$).

Nucleus	ρ^{para}_{calc}	ρ^{para}_{exp}	$\Delta\rho$
Me$_9$	9.87	9.21	0.66
Me$_{10}$	1.04	1.67	-0.63
3	0.57	4.73	-4.16
4a	0.45	3.42	-2.97
4b	0.77	3.96	-3.19
5	1.66	3.48	-1.82
8a	13.46	13.16	0.30
8b	1.59	0.84	0.75

^{133}Cs NMR spectra

To further demonstrate that in Cs[Ln(hfbcv)$_4$] complexes Cs^+ does not occupy a precise geometric position with respect to Ln^{3+} magnetic anisotropy tensor, we recorded ^{133}Cs spectra for CsLa(hfbc)4 and CsPr(hfbc)4 and we observed a paramagnetic shift of 15.3 ppm for Cs, which is in agreement with an estimation of its pseudocontact shift, based on the solution structure of this family of complexes.[S6]

Exchange kinetics

EXSY spectrum of Cs[Nd(hfbcv)$_4$] with a mixing time of 450 msec, displaying exchange cross peaks between all paramagnetically shifted signals and those of the free ligand can be employed to calculate the exchange rate between bound and free ligands.

Selecting three pairs of exchange patterns (proton **3** which in bound/free form falls at 8.19/6.12 ppm, proton **5** falling at 5.51/3.67 ppm and proton **8b** falling at 5.93/4.60 ppm, all of which are well-separated from any interfering signals), we quantified diagonal and cross peak volumes, which were analyzed through the EXSYCalc routine;[S7] the direct and reverse rate constants resulted to be 6x10^{-2} and 1x10^{-2} sec^{-1}.

Tris/*tetrakis* recognition experiment

The biphasic protocol was the only one affording a tris/tetrakis mixture. The signals of the two species can be assigned through standard bidimensional homo and hetero-correlation experiments. The DMSO experiment (see main text), is a quick way to distinguish them unambiguously.

Table S5: μL of added DMSO to the mixture of *tris*+*tetrakis* ($Pr(hfbcv)_3$+$[Pr(hfbcv)_4]^-$), molar ratio of DMSO/(tris+tetrakis) and molar ratio of *tris*/*tetrakis*.

DMSO/μL	DMSO/(*tris*+*tetrakis*)	*tris*/*tetrakis*
0	0	3.0
1	3.4	3.9
2	6.7	5.5
5	16.9	9.8
10	33.7	13.8

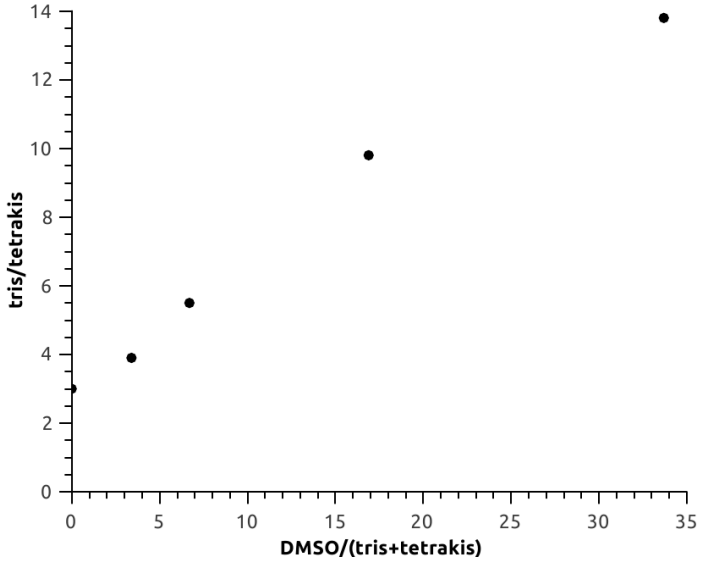

Figure S14: DMSO/(*tris*+*tetrakis*) molar ratio against *tris*/*tetrakis*.

The analysis of the paramagnetic shifts of the *tris* species during the titration with DMSO reveals that the structure of $Pr(hfbcv)_3$ is not deeply affected by axial coordination to water or to DMSO and that the change of the resonance shifts is mainly due to a variation of the anisotropy of the magnetic susceptibility tensor of the Pr complex, as shown by the good linearity (R^2>0.99) obtained plotting δ^{para} at various DMSO concentrations against δ^{para} of the complex before adding DMSO.

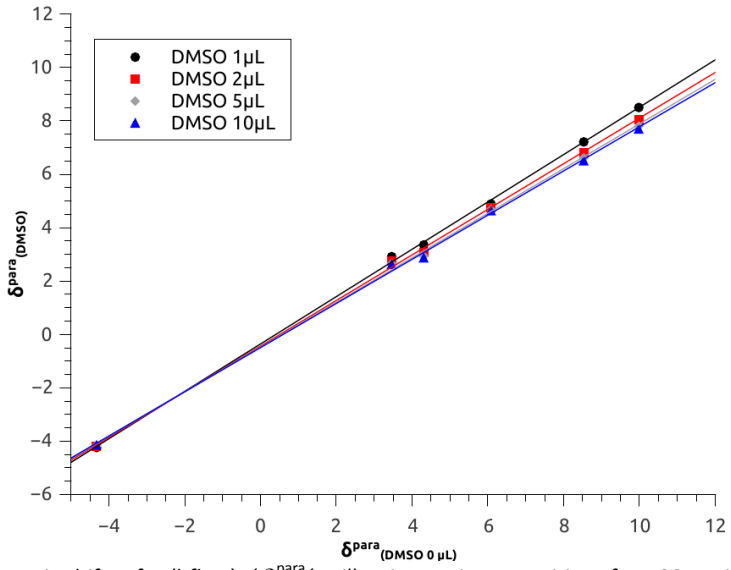

Figure S15: ^{1}H-NMR paramagnetic shifts of Pr(hfbcv)$_3$ ($\delta^{para}(Pr,i)$) at increasing quantities of DMSO against ($\delta^{para}(Pr,i)$) at DMSO=0.

Concerning this last experiment, as discussed in the paper, we found that the ^{1}H and ^{13}C-NMR signals of Pr(hfbcv)$_3$ and [Pr(hfbcv)$_4$]$^-$ are distinct because of the different magnetic susceptibility anisotropy brought about by the different ligand field in the two complexes and also because of the different orientation of the ligand hfbcv with respect to the principal symmetry axis (C_3 or C_4), which is responsible for different geometric factors for each nucleus. In Pr(hfbcv)$_3$, the lanthanide formally has coordination number CN = 6, calling for the involvement of further donor species to saturate the Pr^{3+} sites, which are typically above 7. Generally, for *tris* diketonates of formula LnL$_3$, the exchange equilibrium of a further monodentate ligand at the axial position falls in the fast regime, i.e. the exact frequencies of all resonances of the complex itself and of the axially bound ligand are a function of the total concentration and moreover they are dependent on the solution composition. More specifically, they are sensitive to the relative proportion of competing ancillary ligands. In commercial CD_3CN, the axial coordination site of LnL$_3$ can be efficiently occupied by the residual water. This is the reason for finding the water resonance displaced from the usual value of δ^{free}_{w} = 2.13 ppm. In the case of Pr^{3+}, which is characterized by a negative Bleaney's factor C_j, any axially bound ligand is expected to be upfield displaced, which is exactly what we observed.

In this case, one may try to grossly evaluate the mole fraction of water-bound Pr(hfbcv)$_3$, x^w. To this end, we can take into account that the ^{1}H shift for axially-bonded water, δ^{bound}_{w} (with a Pr-O$_w$ distance =2.5 Å and using a magnetic anisotropy D = 659 Å^3/ppm, as determined through PERSEUS analysis) can be estimated to be δ^{bound}_{w} = 67ppm and that the normalized integral ratio between water and Pr(hfbcv)$_3$ is 6.82, which yields x^w = 0.19.
The fact that upon adding DMSO the water resonance shifts towards its δ^{free}_{w}, demonstrates that DMSO is a stronger ligand than H_2O, as we had put forward. The *tris* complex must then be considered of formula Ln(hfbcv)$_3$·X (X = H_2O, DMSO).

MALDI-TOF MS characterization

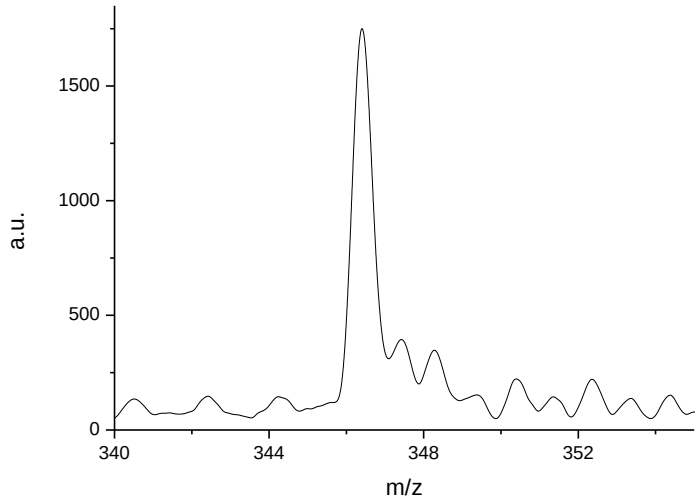

Figure S16: MALDI-TOF mass spectrum of hfbcvH.

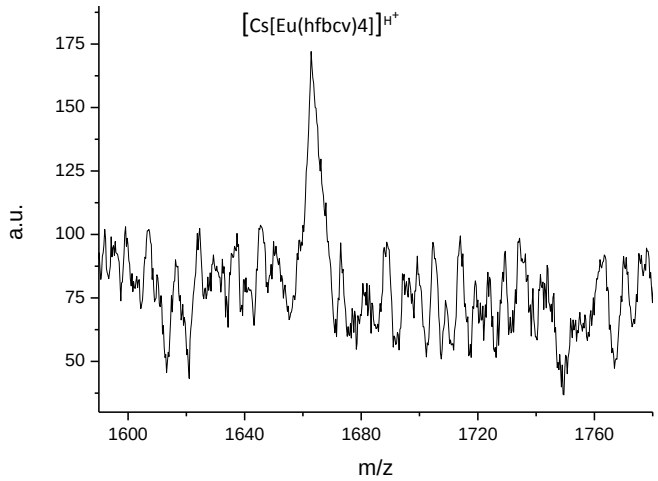

Figure S17: Positive MALDI-TOF mass spectrum of $Cs[Eu(hfbcv)_4]$.

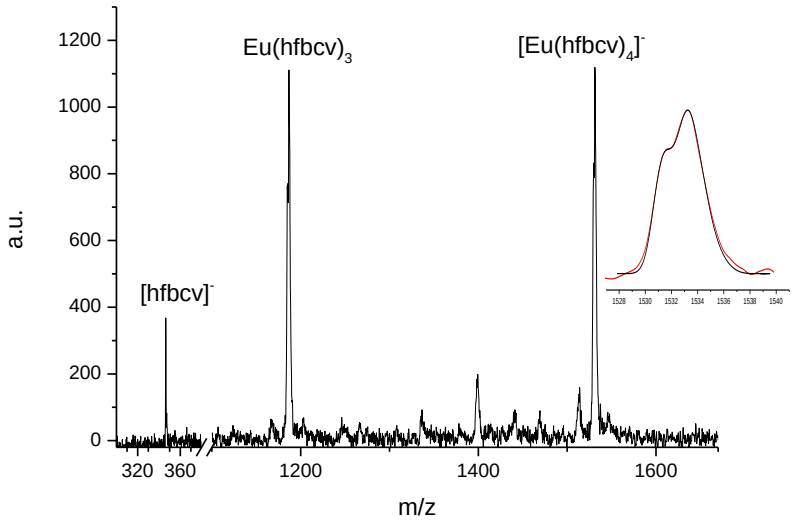

Figure S18: Negative MALDI-TOF mass spectrum of $Cs[Eu(hfbcv)_4]$. In the inset, for the sake of comparison, the experimental isotopic cluster peaks of $[Eu(hfbcv)_4]^-$ species (red line) and its simulated isotopic distribution (black line), FWHM = 860, is reported. The peak in the inset was smoothed using Savitzky-Golay filter.

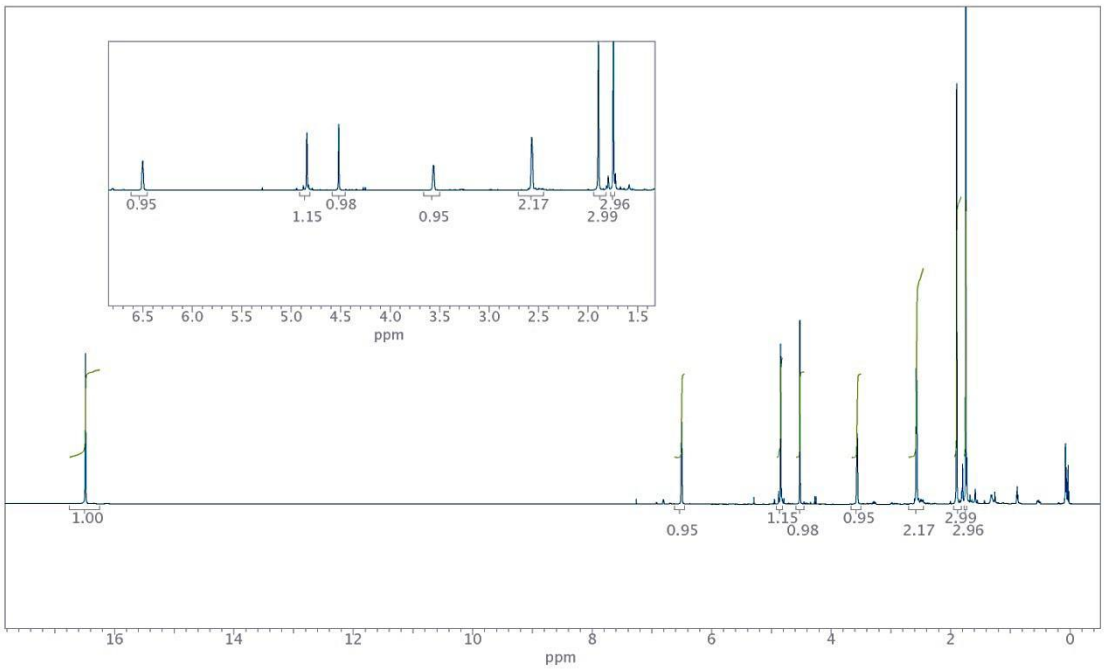

Figure S19: ^{1}H-NMR spectrum of the ligand hfbcvH in $CDCl_3$.

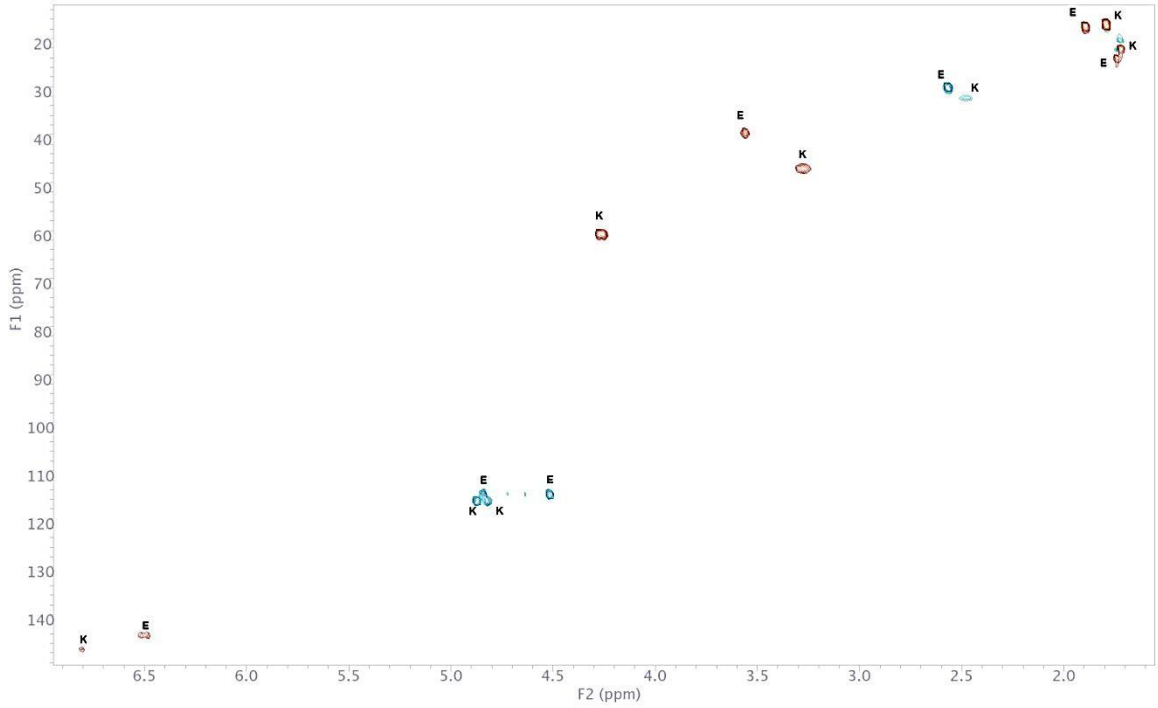

Figure S20: HSQC spectrum of the ligand hfbcvH in $CDCl_3$, both keto (**K**) and eno (**E**) form are visible.

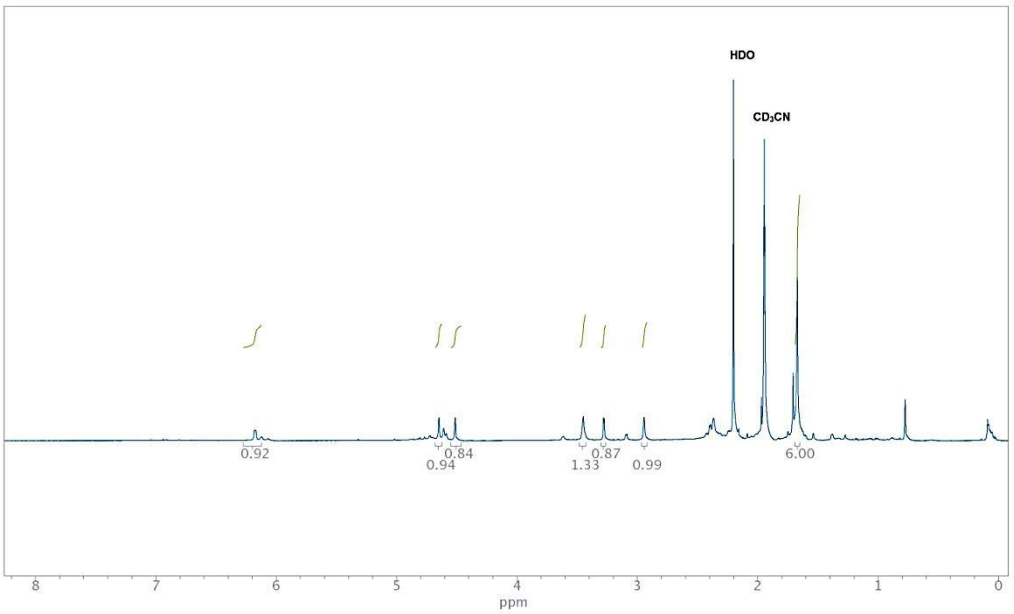

Figure S21: ^{1}H-NMR spectrum of Cs[La(hfbcv)$_4$] in CD_3CN.

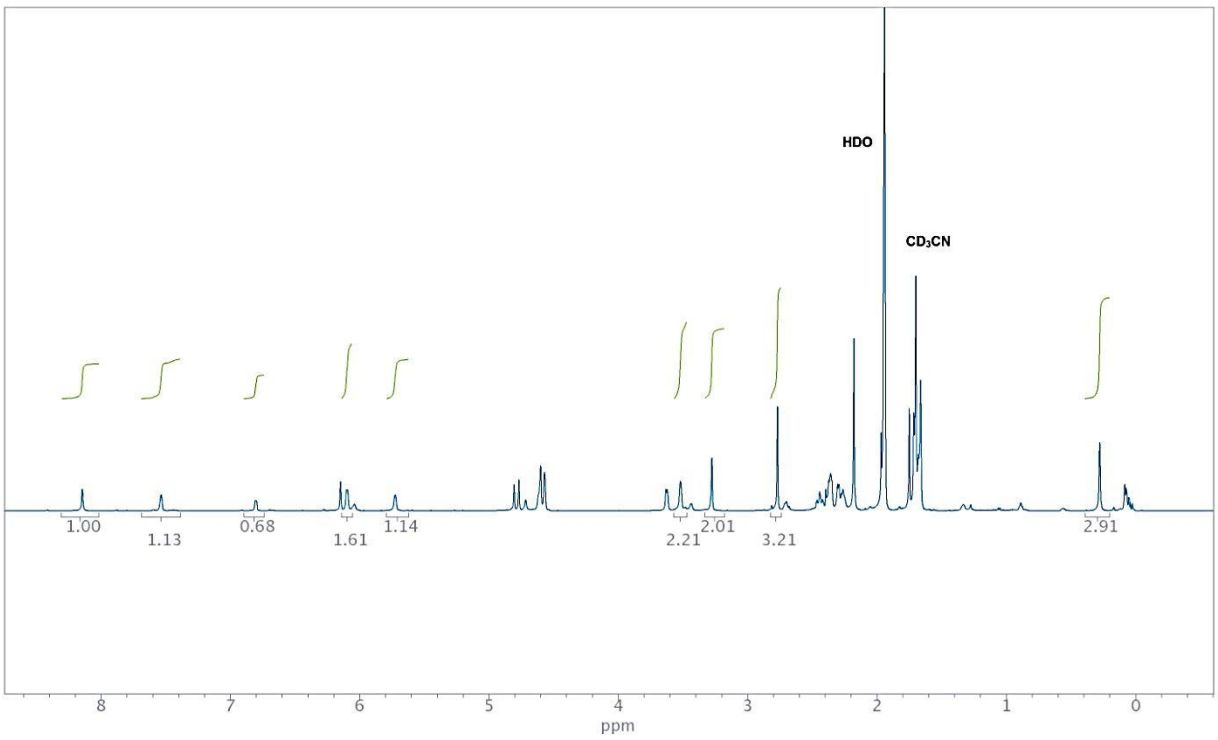

Figure S22: ^{1}H-NMR spectrum of Cs[Ce(hfbcv)$_4$] in CD_3CN.

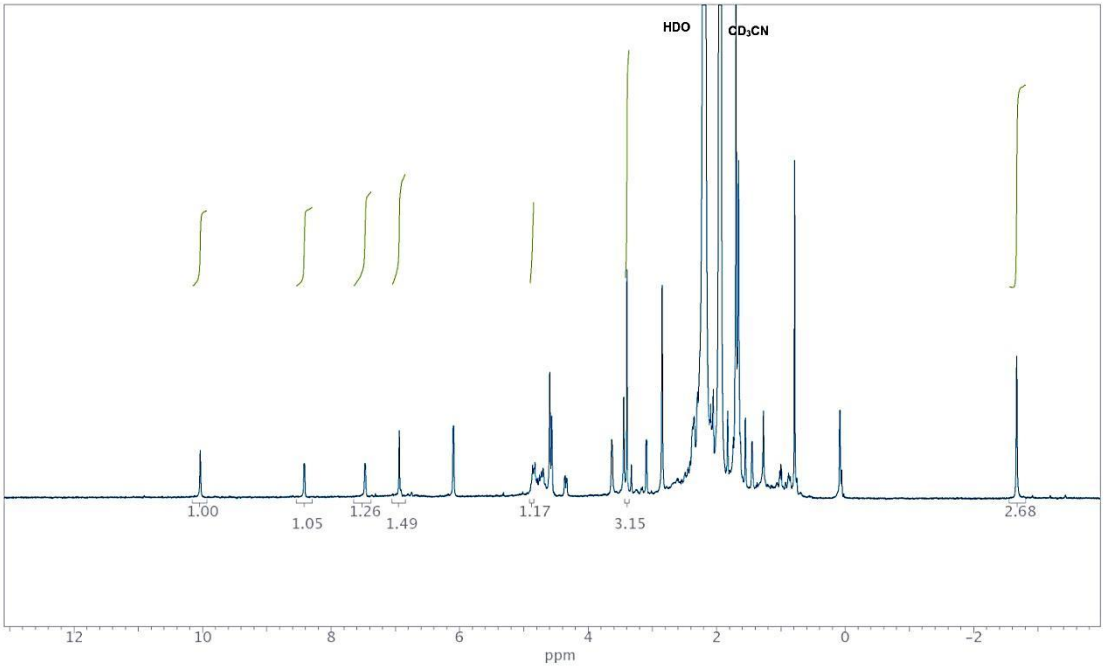

Figure S23: ^{1}H-NMR spectrum of Cs[Pr(hfbcv)$_4$] in CD_3CN.

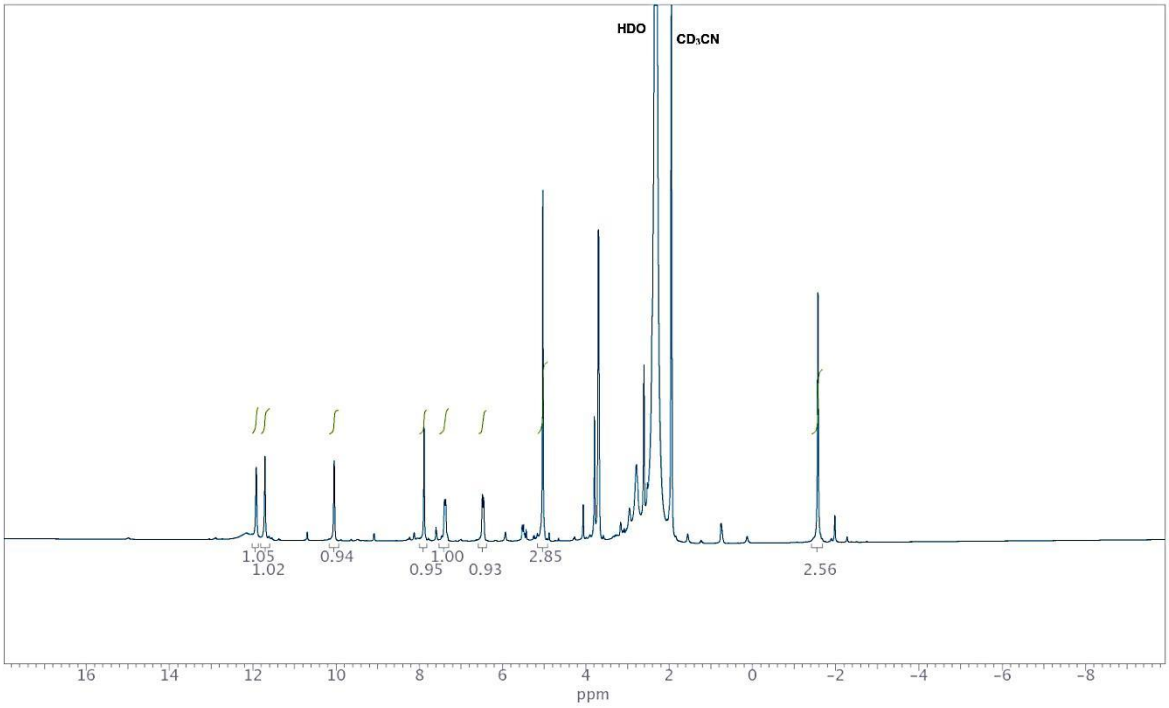

Figure S24: ^{1}H-NMR spectrum of Pr(hfbcv)$_3$ in CD_3CN (after the addition of DMSO).

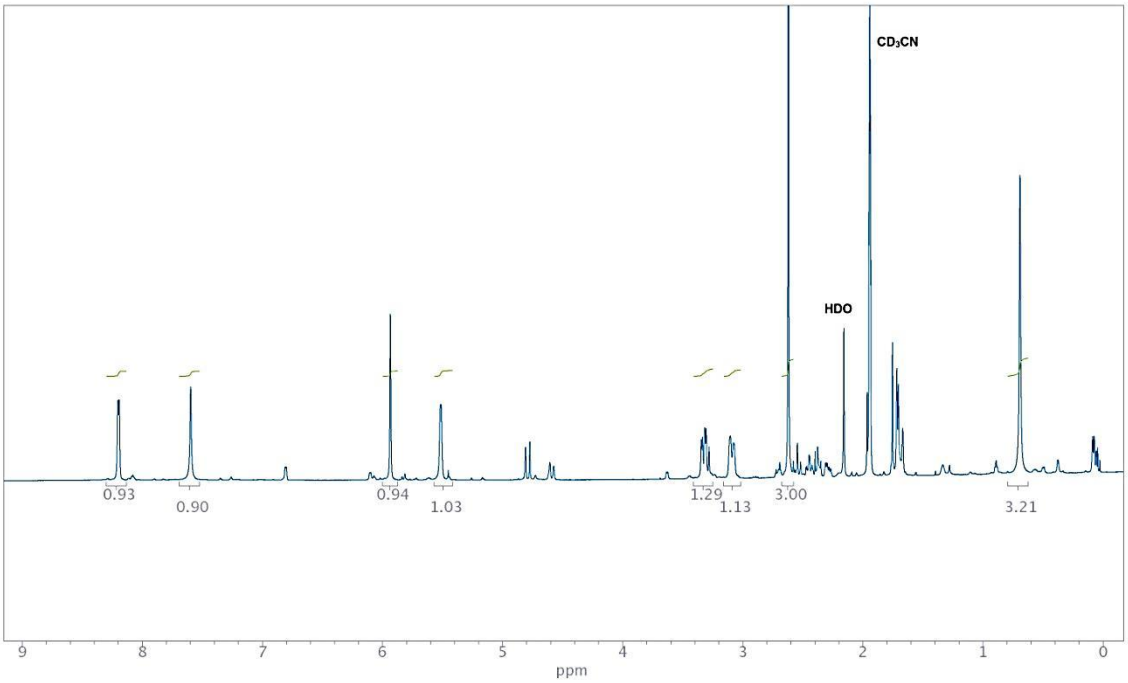

Figure S25: ^{1}H-NMR spectrum of Cs[Nd(hfbcv)$_4$] in CD_3CN.

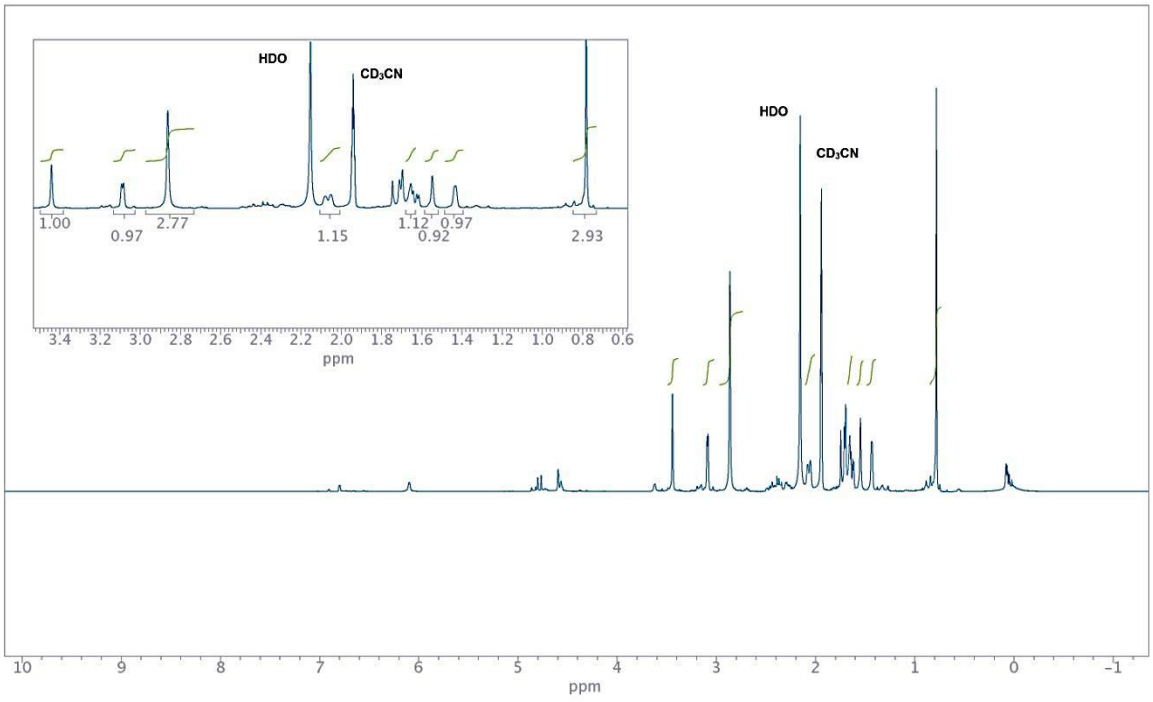

Figure S26: ^{1}H-NMR spectrum of Cs[Eu(hfbcv)$_4$] in CD_3CN.

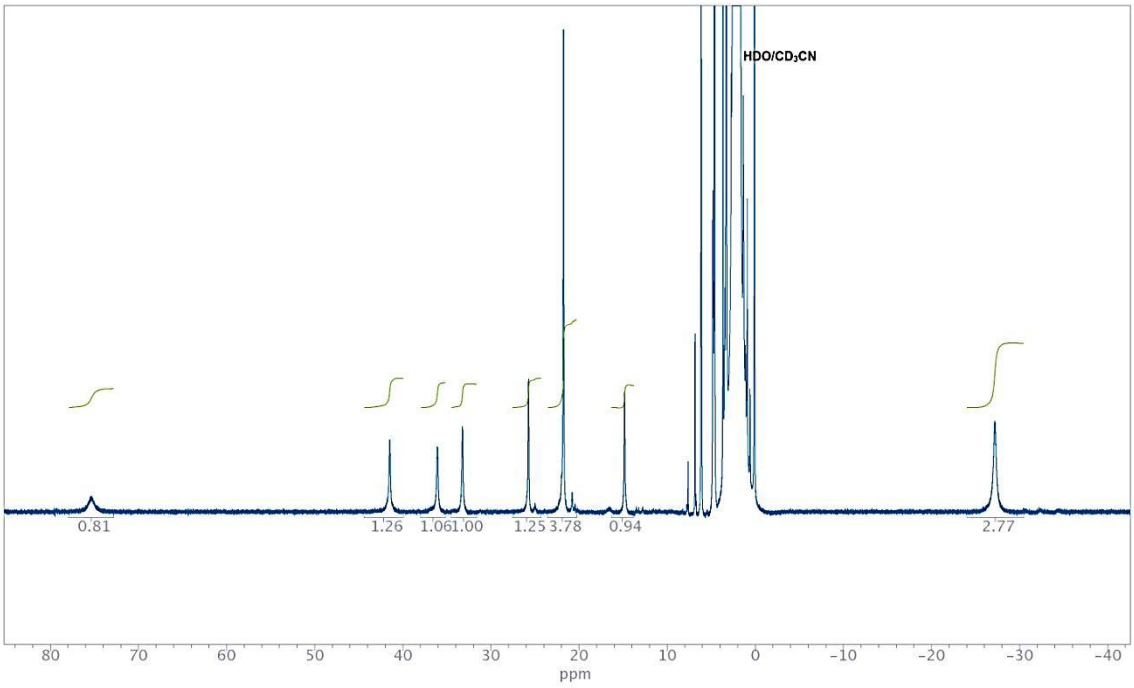

Figure S27: ^{1}H-NMR spectrum of Cs[Tb(hfbcv)$_4$] in CD_3CN.

Additional references

S1 E. Castiglioni, S. Abbate, G. Longhi, *J. Appl. Spectrosc.*, 2010, **64**, 1416–1419.

S2 E. Castiglioni, S. Abbate, F. Lebon, G. Longhi, *Chirality*, 2012, **24**, 725-730.

S3 Gaussian 09, Revision D.01, M. J. Frisch, G. W. Trucks, H. B. Schlegel, G. E. Scuseria, M. A. Robb, J. R. Cheeseman, G. Scalmani, V. Barone, B. Mennucci, G. A. Petersson, H. Nakatsuji, M. Caricato, X. Li, H. P. Hratchian, A. F. Izmaylov, J. Bloino, G. Zheng, J. L. Sonnenberg, M. Hada, M. Ehara, K. Toyota, R. Fukuda, J. Hasegawa, M. Ishida, T. Nakajima, Y. Honda, O. Kitao, H. Nakai, T. Vreven, J. A. Montgomery, Jr., J. E. Peralta, F. Ogliaro, M. Bearpark, J. J. Heyd, E. Brothers, K. N. Kudin, V. N. Staroverov, R. Kobayashi, J. Normand, K. Raghavachari, A. Rendell, J. C. Burant, S. S. Iyengar, J. Tomasi, M. Cossi, N. Rega, J. M. Millam, M. Klene, J. E. Knox, J. B. Cross, V. Bakken, C. Adamo, J. Jaramillo, R. Gomperts, R. E. Stratmann, O. Yazyev, A. J. Austin, R. Cammi, C. Pomelli, J. W. Ochterski, R. L. Martin, K. Morokuma, V. G. Zakrzewski, G. A. Voth, P. Salvador, J. J. Dannenberg, S. Dapprich, A. D. Daniels, Ö. Farkas, J. B. Foresman, J. V. Ortiz, J. Cioslowski, and D. J. Fox, Gaussian, Inc., Wallingford CT, 2009.

S4 L. Di Bari and P. Salvadori, *Coord. Chem. Rev.*, 2005, **249**, 2854-2879.

S5 S. Di Pietro, S. Lo Piano, L. Di Bari, *Coord. Chem. Rev.*, 2011, **255**, 2810–2820.

S6 S. Di Pietro and L. Di Bari, *Inorg. Chem.*, 2012, **51**, 12007-12014.

S7 J. C. Cobas, M. Martin-Pastor, EXSYCalc Version 1.0, Mestrelab Reasearch.